AIAA SciTech Forum
8-12 January 2024, Orlando, FL
AIAA SCITECH 2024 Forum

10.2514/6.2024-0823

Concept for Scalable Mesh Reflector Antennas Assembled in Space

Jong-Eun Suh *, and Sahangi P. Dassanayake[†]
California Institute of Technology, Pasadena, California, 91125, United States

Mark W. Thomson[‡]
Tendeg LLC, Louisville, Colorado, 80027, United States

Sergio Pellegrino[§]
California Institute of Technology, Pasadena, California, 91125, United States

Conventional deployable design approaches have size limitations due to launch fairing size. This study presents a design study of in-space assembled reflectors. Their geometry and structural design focus on mass efficiency. Scaling study of the mass and stowed volume of the reflectors establishes the feasibility of launching reflectors with aperture diameters up to 200m using commercial launch vehicles. A reflector assembly concept is proposed, that enables the assembly of large reflectors with a centralized robotic assembly factory. The proposed scheme is then demonstrated with a lab-scale prototype, proving the feasibility of the assembly concept.

I. Introduction

Deployable space-based mesh reflector antennas are well established for aperture diameters of 10 - 20 m [1–3]. A standard deployable architecture is the AstroMesh consisting of doubly curved cable nets supported by a deployable perimeter truss [4, 5]. This specific reflector design has been successful in achieving mass and volume efficiency [6–9].

Deployable architectures have to meet the mass and volume constraints of launch vehicles, as well as the load constraints imposed by the dynamic environment during the launch. It is not feasible to launch structures with stowed heights greater than 20 m with existing launch vehicles [10]. This leads to the need for building extremely large structures in space.

Many researchers have studied in-space assembly (ISA) technologies. ISA requires the following: modularization of the functional elements and strategies to assemble separate modules in space. Developing ISA architectures will enable new ways of building large structures in space environment [11, 12]. Concepts for building large functional structures with ISA [10] include RAMST [13] and ALMOST [14], two concepts for modular space telescopes assembled in space.

In the current study, we consider building in space reflectors with a specific architecture, Fig. 1. The reflector consists of two identical cable nets approximating a paraboloid. A reflective surface is attached to the front net. Tension ties are installed between the front and rear net, applying prestress to the cables. Both front and rear nets are attached to a perimeter truss. The design of the reflector is similar to the deployable AstroMesh, but the concept implementation now enables assembly in space as opposed to deployment from the stowed configuration. This paper is organized as follows: we start by designing the geometry and structure of the reflector. The mass and stowed volume are then calculated for apertures up to 200 m, to evaluate the launch limits of the proposed reflector. Then we propose the in-space assembly scheme that enables the assembly of large reflectors with a centralized robotic system. A lab-scale prototype is used to demonstrate the proposed assembly procedure.

*Postdoctoral Researcher, Graduate Aerospace Laboratories, AIAA Member.
[†]Graduate Student, Graduate Aerospace Laboratories, AIAA Student Member.
[‡]Chief Technology Officer.
[§]Joyce and Kent Kresa Professor of Aerospace and Civil Engineering, Graduate Aerospace Laboratories, AIAA Fellow.

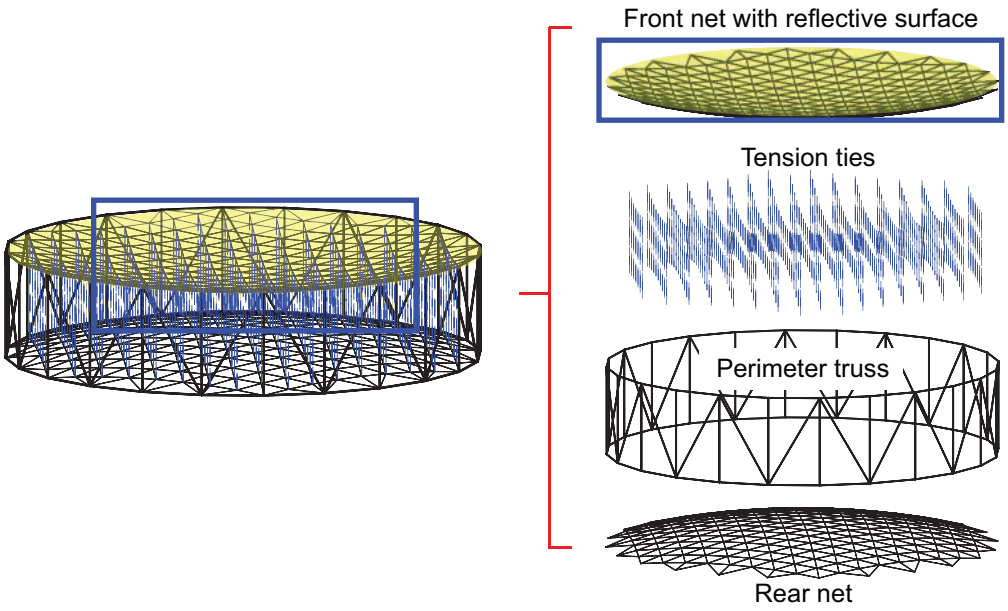

Fig. 1 Structural components of reflector assembled in space

II. Geometry and Structural Design

A. Geometry design

The reflective surface is typically designed to be parabolic to maximize the antenna's directivity. Figure 2a shows a circular paraboloid surface with diameter D, focal length F, apex height s_0, and rim height $s_0 + s$. One of the critical design parameters affecting the geometry of the parabolic reflector is its F/D ratio; the higher F/D ratio, the shallower the paraboloid surface. In this study, we consider reflector designs with $F/D = 1.0$.

The paraboloid surface of the reflector is approximated by triangular facets of size L, forming a hexagonal tessellation, Fig. 2b. Faceting of the paraboloid surface causes a surface error; thus, the size of the triangles is determined by considering the surface RMS error requirement. The faceting error of a spherical surface with radius, R, is generally given by [15]:

$$\delta_{facet} = \frac{L^2}{8\sqrt{15}R} \tag{1}$$

Any given axisymmetric paraboloid can be approximated by a spherical cap [16], and the following relationship between R and the design parameters of the paraboloid is used to calculate the facet size:

$$R = 2F + \frac{D^2}{32F} \tag{2}$$

An operational radio frequency of 10 GHz is assembled in the current study, which sets the surface RMS error requirements to 0.6 mm. The surface error calculation assumed that the faceting error is the only factor inducing the surface RMS error (i.e., $\delta_{RMS} = \delta_{facet}$); therefore, the maximum allowable facet size for the given diameter is then obtained by using Eqs. (1) and (2). The maximum allowable size of the facet increases proportionally to $\sqrt{D}$ as the diameter of the reflector increases.

Figure 2b presents the cable net configuration. Once the facet size is determined for a reflector of the required size, the number of subdivisions of the reflective surface, n, is calculated using the relationship: $n = 0.5D/L$. The front and rear nets include the cables forming a tessellation of equilateral triangles in the xy plane (black solid lines in Fig. 2b) and the cables connected to the perimeter truss (red solid lines in Fig. 2b), called *Inner Net* and *Boundary Net*, respectively. The intersecting nodes in the inner net are denoted as *free nodes*. They are connected by tension ties, applying tension forces between the front and rear nets and maintaining the parabolic surface. The geometry of the

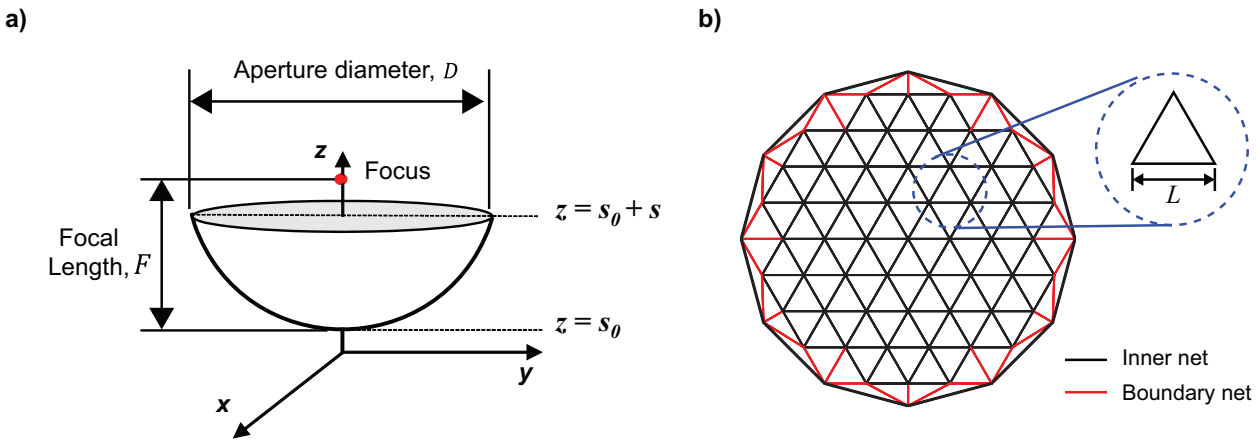

Fig. 2 Parabolic surface: a) schematic drawing of a paraboloid, and b) cable net configuration

inner net is uniquely determined by the facet size. The geometry of the rest of the cable net provides a transition from the inner net to the perimeter truss. In this study, the perimeter truss has been designed to be half-density of the net, which means a single batten supports three free nodes with boundary cables. The lengths of the longerons, battens, and diagonals were determined based on the designed net geometry.

B. Structural design

For the reflective surface of the in-space assembled reflector, a typical knitted metallic mesh is used, with areal density $\rho_{mesh} = 0.025$ kg/m^2. The mesh requires a biaxial prestress, σ, to prevent ohmic losses during operation, which is set to 5 N/m.

The cables composing the front and rear nets of the reflector are thin CFRP strips of M55J carbon fiber [17] in a thermoplastic matrix with overall density $\rho_{CFRP} = 1786$ kg/m^3, and modulus $E_{CFRP} = 325.4$ GPa. The cross-section of the CFRP strip is a rectangle, where the width and thickness are 6 mm and 150 μm, respectively. To prevent bowing of the cables, the minimum pre-tension is set to $P_{min} = 10\,\sigma L_{max}$.

The tension ties are the components applying the tension to the cable nets. The tension tie force distribution with respect to the installed location is optimized to achieve a nearly uniform prestress distribution along the cables.

Owing to the pre-tension applied by the tension ties, the struts of the perimeter truss are subjected to relatively high compression. The cross-section of each type of strut (i.e., longerons, battens, and diagonals) is a circular tube, where the diameter and thickness of the tube are determined to prevent buckling failure. Given that the longerons are subjected to the largest compression, the size of the longerons is determined first. The batten and diagonal are designed based on the longeron size. For simplicity, the thickness of the longeron is fixed at 1 mm for all reflector apertures; only the longeron's radius is considered a design variable. The radius of the longeron cross-section is determined by setting a margin of 2 against buckling. The battens and diagonals are designed to have the same diameter as the longeron, and their thicknesses are determined based on the same buckling criterion but with the corresponding level of compression applied to each component.

The joints are assumed to be made of the same CFRP as the cables and struts. The size of the joints is designed to be proportional to the size of the tubes and scales with the reflector diameter.

III. Scaling of mass and stowed volume

To assess the launch limits of the proposed reflector, the structural mass, and the stowed volume are calculated for aperture sizes from $D = 10$ m to 200 m. The mass and volume of the robotic assembly facilities have not been considered yet.

To calculate the total mass of the reflector, the mass of the cable net (m_n), metallic mesh (m_{mesh}), struts (m_{truss}), tension ties (m_{tt}), and joints (m_j) are considered:

$$m_{total} = m_n + m_{mesh} + m_{truss} + m_{tt} + m_j \tag{3}$$

The mass of each component of the reflector is calculated based on the structural design described in Section II. The mass of the cable net, m_n, is calculated from

$$m_n = \rho_n A_n \sum L_{ij} \tag{4}$$

the material density, cross-sectional area, and total length of the cables.

It is assumed that the metallic mesh covers the complete surface of the front net. The mass of the perimeter truss is calculated based on the structural design of longeron, batten, and diagonal described in Section II. The mass of tension ties and mesh seams, m_{tt}, is assumed to be twice m_{mesh}.

To evaluate the volume of the reflector parts, the following storage strategy for the structural components was adapted: Both front and rear nets are first fabricated and assembled with tension ties and metallic mesh. This net assembly is then compacted. The compacted volume is calculated and assumed to be 20 times its material volume. The struts of the perimeter truss are assumed to be made by cutting a deployable omega beam, flattened and coiled on a mandrel. The dimension of the strut spools is estimated as follows: the height of the core mandrel is the same as the flattened width of the strut, and the core diameter is designed to be the same as the height. When the flattened strut is coiled around the core, the diameter of the spool becomes larger; the maximum diameter of the spool is set to four times the core diameter. Therefore, the total number of strut spools is calculated by considering the total length of the struts. The volume of the joint stack is calculated from the envelope of the joint. Once the total volume of the components of the truss has been obtained, the overall diameter and height of the components are derived by assuming that all the components are compactly arranged inside a cylindrical envelope with height equal to twice the diameter.

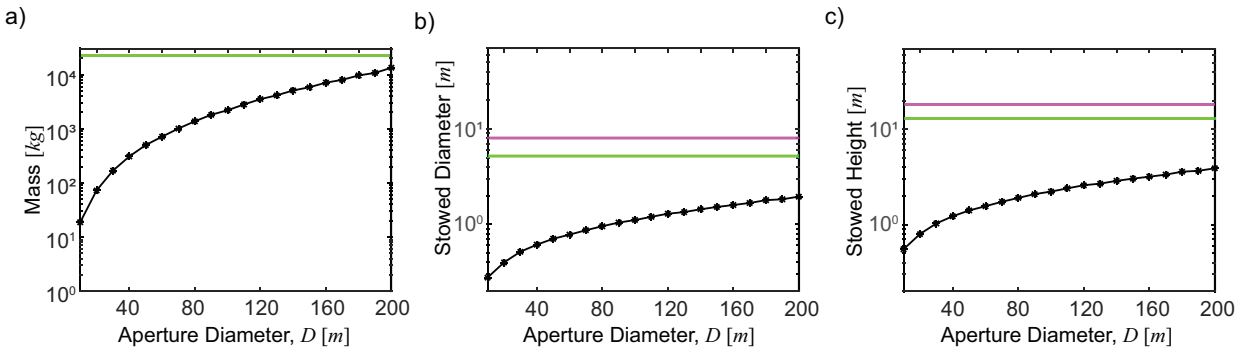

Fig. 3 Mass and volume scaling plot (green: Falcon Heavy limits, pink: Starship limits): a) mass of reflector, b) stowed diameter, and c) stowed height

Figure 3 shows the mass (a), stowed diameter (b), and stowed height (c) of the reflector components for the aperture diameter range of 10 m to 200 m. The total mass and stowed volume were found to scale approximately quadratically with diameter.

Two launch vehicles are selected to evaluate the availability of launchers for reflectors with a large aperture: Falcon Heavy [18], and Starship [19]. In Fig. 3b and Fig. 3c, the pink and green colored solid lines represent the payload limits for Starship and Falcon Heavy, respectively. Given the maximum payload mass to geostationary transfer orbit (GTO) is 26,700 kg for Falcon Heavy [18], two current state-of-the-art launch vehicles, Fig. 3b and Fig. 3c indicate capability to launch the proposed in-space assembled reflectors up to around $D = 200$ m. Considering the volume inside the fairing, the stowed diameter and height of the structural components are well below the limits, even for $D = 200$ m. Therefore, a single launch can deliver a reflector larger than 200 m to space.

IV. In-space Assembly Facility

A. In-space assembly concept

Figure 4 shows schematically the proposed in-space assembly operation. The assembly facility is called the truss builder. It is folded and stowed in the launch vehicle. The structural components (i.e. struts, joints, and net) are packed and stored inside the folded truss builder, ready to be assembled when the truss builder is fully deployed (Fig. 4a). After

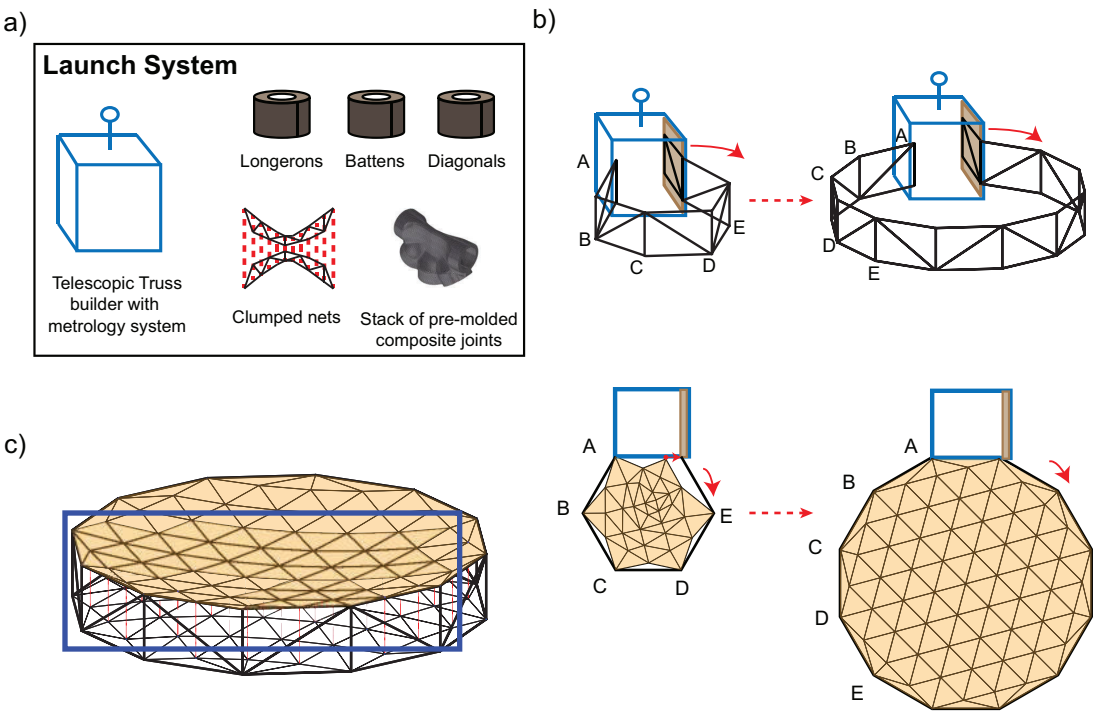

Fig. 4 In-space assembly scheme: a) components stowed in the launch vehicle, b) building the perimeter truss while attaching the cable nets, and c) assembled reflector

launching to the target orbit, the truss builder is deployed before assembly commences. The perimeter truss is assembled by a mechanism inside the truss builder (Fig. 4b). Each bay of the truss is constructed inside the truss builder, and released outside; thus, the diameter of the perimeter truss grows in size as more bays are added. The slack nets are attached to the joints of the perimeter truss while each bay is constructed and released (Fig. 4c). Note that the metallic mesh is attached to the front net before launch and is compacted together with it; therefore, the antenna assembly is completed once the truss builder finishes the last bay release and the last node of the cable net has been attached.

B. Truss builder

Figure 5 presents the step-by-step process for building the truss. As described in the previous section, the perimeter truss is assembled and released into the space one bay at a time. The major components of the truss builder are as follows: sliding assembly plate, joint-strut assembly robot, cable retractor, and net attachment robot. The general process of bay construction is as follows: the joint-strut assembly robot picks up the joints and struts from the storage, and installs them on the assembly plate to build a single bay of the truss (red lines in Fig. 5). The assembly plate is pushed out of the truss builder, the bay is released, and the assembly plate is retracted. Released bays are represented in blue lines in Fig. 5. During the first bay construction, a cable is attached to the forward joints of the bay. Once the second bay is released, this cable is retracted to bring the tip joints to the right-hand side of the truss builder. After fixing the tip joints to the truss builder, the bay construction process is repeated until the perimeter truss has been completed. Note that the boundary nodes of the net are attached to the joints before each bay is pushed out. To ensure the stability of the structure during the assembly process, the joints are designed to be elastically deformable to maintain a near-circular shape for the constructed bays.

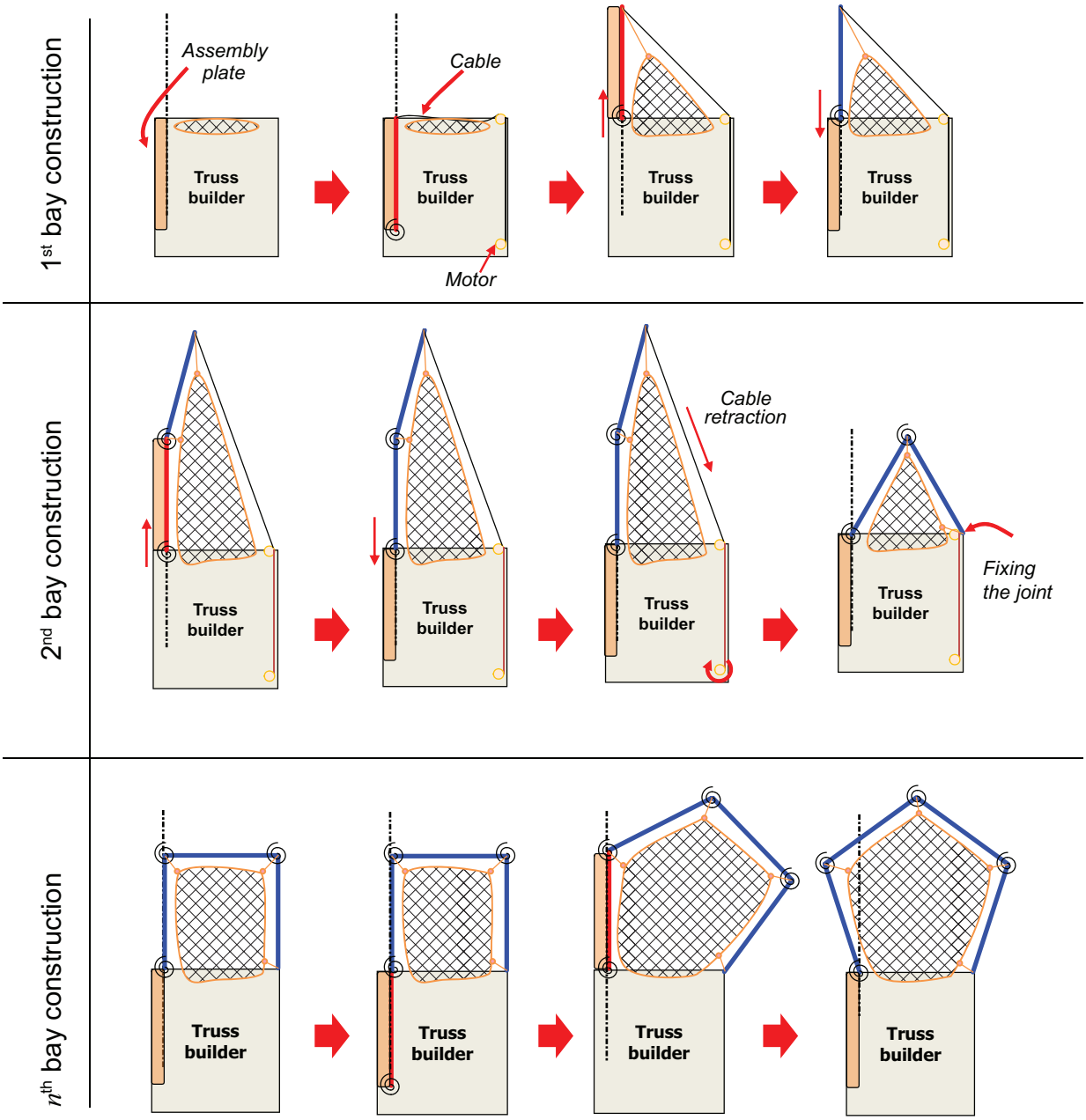

Fig. 5 Truss building procedure: first, second, and n^{th} bay construction steps

V. Proof of concept demonstration

A. Demonstration plan

In order to assess the feasibility of the proposed in-space assembly process, prototypes of each component and of the truss builder have been manufactured and are being demonstrated in the laboratory. Figure 6 shows a CAD illustration of the target reflector and the truss builder. The assembly demonstration aims to construct a reflector with 1.4 m diameter (Fig. 6a). The number of subdivisions of the reflective surface is $n = 4$, which requires 12 bays for the perimeter truss. Since the truss builder itself replaces the last bay of the perimeter truss, 45 struts (i.e., 22 longerons, 12 battens, and 11 diagonals), and 24 joints are required in total. The length of batten, longeron, and diagonal composing the perimeter truss are calculated based on the geometry of a reflector with $F/D = 1.0$.

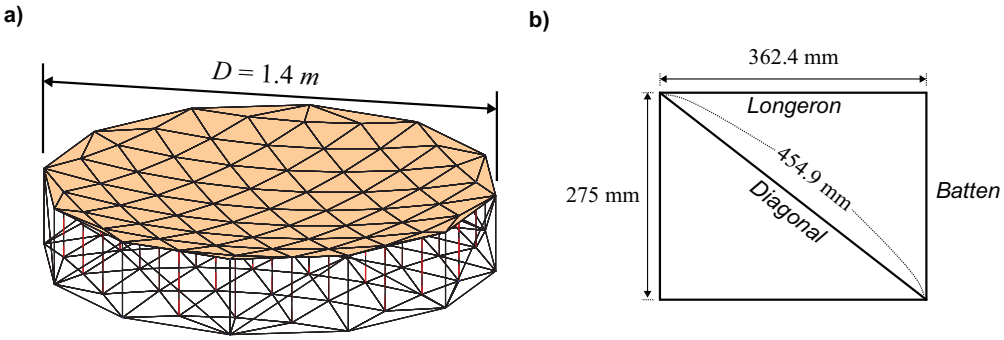

Fig. 6 Lab-scale demonstration: a) target reflector, and b) dimension of a single bay

B. Prototype design and manufacturing

1. Perimeter truss

The structural components of the reflector are designed to be modular and able to be assembled by a simple robot to reduce the system's complexity. Figure 7a shows a CAD image of the prototype joint for the perimeter truss. Each joint is composed of two separate parts, which are 3-D printed (CraftBot Plus Pro, Craftbot USA) with PLA (Polylactic Acid). The two parts are assembled with bearings to enable relative rotation and two torsional springs are attached to the shaft to provide rotational stiffness. Four recessed surfaces provide a housing for the longerons, batten, and diagonal that are attached to the joint; each recess contains a small permanent magnet, which helps align struts to the slots during the bay construction process. The connection between a joint and a strut is presented in Fig. 7b. Each strut is a pultruded composite tube. At both tips of the tube, 3-D printed caps with magnets are attached. The shape of the cap is designed to fit inside the slot on the joint. Note that the dimensions of the slot and the tip of the strut are carefully designed to enable a press-fit to the strut connection; thus, both friction and magnetic attraction hold the strut in place once the joint has been assembled. A circular permanent magnet and two cones on the upper and lower sides of the magnet help guide and attach the joint to the joint mounting fixture on the assembly plate. The manufactured prototypes of the joint, strut, and single bay of the perimeter truss are presented in Fig. 7c.

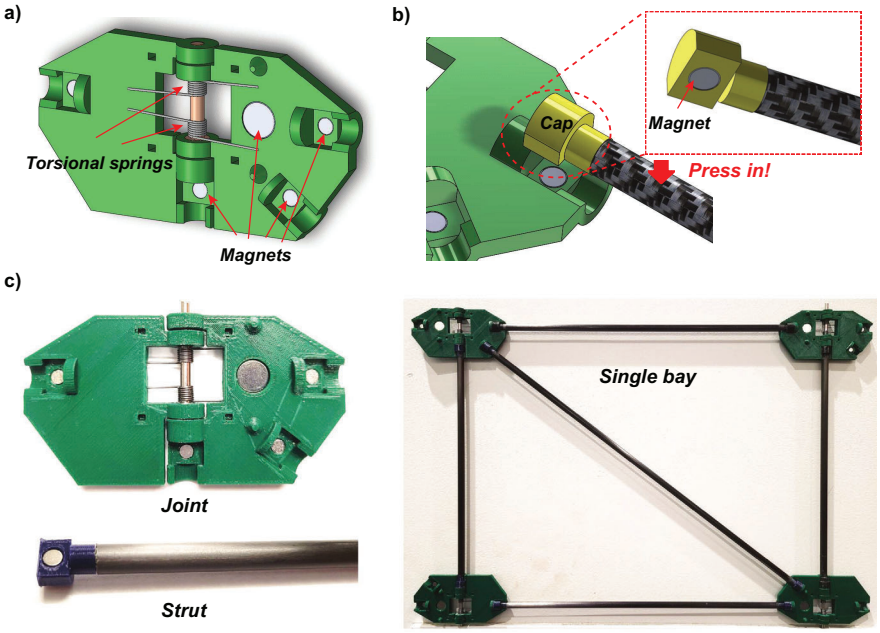

Fig. 7 Prototype design and fabrication: a) CAD drawing of the joint, b) CAD drawing of joint-strut attachment, and c) prototype of joint, strut, and complete bay

2. Joint-strut latching force measurement

Since the strut tip is designed to be press-fitted into the slot, the strut latching forces were measured to select an actuator for the joint-strut assembly robot that provides a sufficient pushing force. Figure 8a shows the latching force measurement setup. Since the robot has to pick up the strut at the center, and then pushes it into the pre-placed joint, the latching force is measured with an Instron materials testing machine that presses the center of a strut sitting on joint slots at both ends.

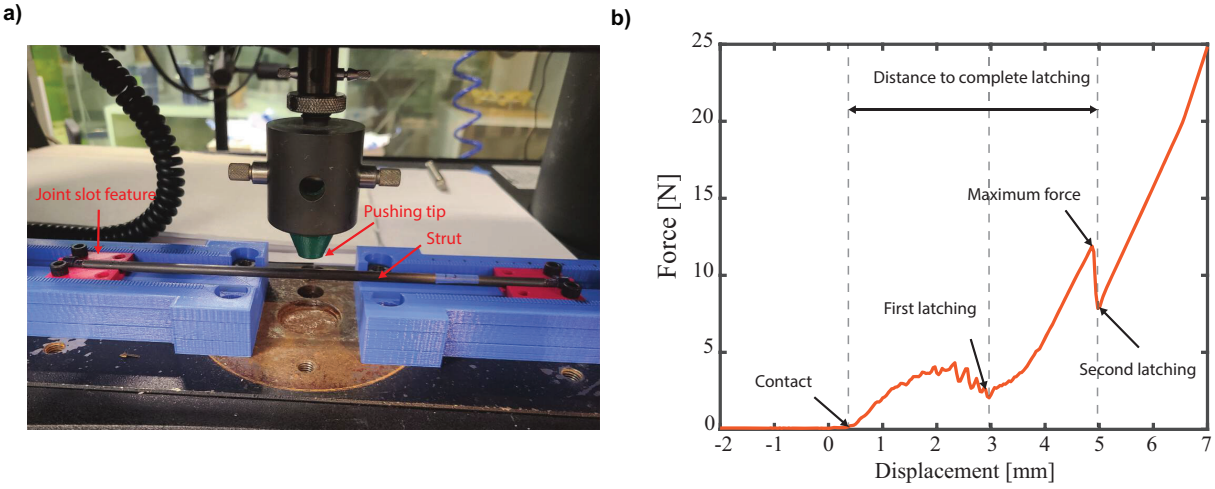

Fig. 8 Strut latching experiment: a) experiment setup, and b) force-displacement curve for a diagonal

Latching force measurements are conducted for all 45 struts (12 battens, 22 longerons, and 11 diagonals), and Fig. 8a shows a representative force-displacement curve measured from one of these tests. In the force-displacement curve, two peaks appear as the strut is being pushed into the joint slots, which correspond to latching events on each joint slot. Based on the latching force measurement result, we calculated the maximum latching force as the maximum peak force before the second latching event and the push distance as the displacement of the tip from the first contact to the second latching. For each type of strut, the average and maximum latching force is calculated and listed in Table 1, along with the average and maximum pushing distance. Based on the latching force measurements, the requirement for the joint-strut assembly robot is that the push actuator should provide force higher than 40 N with a stroke of 9 mm, to achieve a safety factor higher than 1.5.

Table 1 Latching force and pushing distance of struts

	Latching force [N]		Pushing distance [mm]	
Type of strut	Average	Maximum	Average	Maximum
Batten	15.1	22.7	2.84	4.06
Longeron	13.9	26.2	3.59	4.53
Diagonal	13.1	24.5	4.66	5.87

3. Cable net assembly

The cable net assembly in the mesh reflector consists of the front cable net with the mesh, the rear cable net, and tension ties connecting two cable nets; the cable net in the prototype reflector is fabricated by cutting 50 μm thick Kapton film (Kapton HN film, Americal Durafilm) with the cable net pattern calculated for $D = 1.4$ m, $F/D = 1.0$ reflector. Both the front net and the rear net are fabricated with the same geometry, and a nylon knitted mesh is attached underneath the front cable net. A carabiner, shown in Fig. 9a, is attached at each outer node of both the front and rear nets, to connect the cable net assembly to the joints of the perimeter truss. The tension ties are manufactured using extension springs (EIM030D 05 S, Lee Spring Company); both ends of each extension spring are tied with strings, and

connected to the front and rear net, Fig. 9b. The length of the string is designed to provide the required tension to the cable net assembly when the net is fully deployed. Note that the extension springs in the tension tie prototype are sealed within rubber tubes to prevent entanglement when the net is folded and stored in the truss builder. The completed net prototype is fan-folded and stored at the truss builder; the carabiners attached to the outer nodes of the cable nets are sequentially connected to a rod and are attached to a joint as the bay construction is completed inside the truss builder. Figure 9c shows a carabiner attached to a joint shaft by the net attachment mechanism.

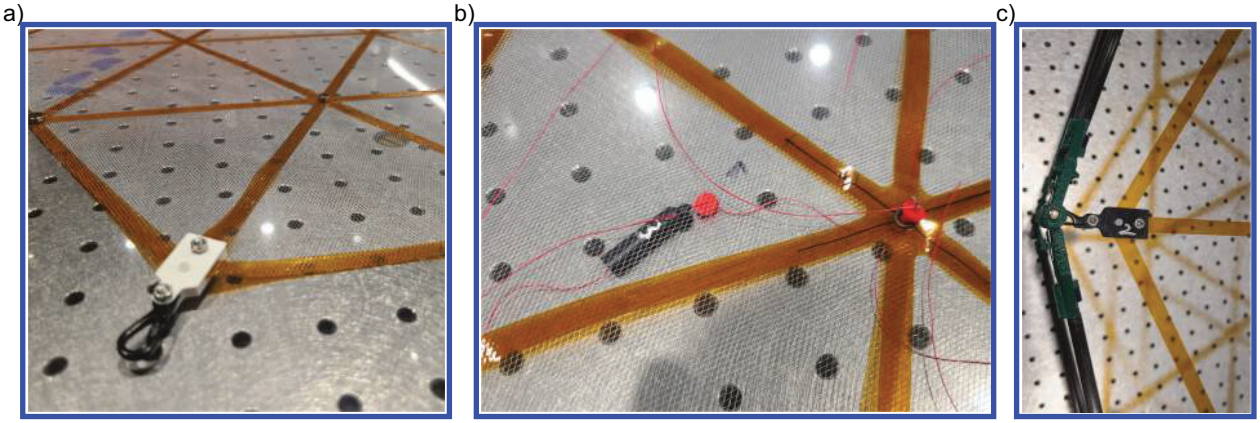

Fig. 9 Cable net prototype: a) carabiner installed at the outer node of cable net, b) tension tie, and c) cable net attached to the truss

4. Truss builder prototype

The truss builder prototype, shown in Fig. 10a, is composed of the sliding assembly plate (brown plate), strut storage, and manipulator. The assembly plate includes four joint mounting plates, each with an electromagnet. Since each joint contains a permanent magnet, during the bay construction, the electromagnet holds the joint on the mounting plate. The manipulator picks up the struts and joints from the storage and places them in the desired location on the assembly plate to build a single bay; this operation requires a 4-DoF (x, y, and z translational, and Rz rotational direction) capable manipulator. The prototype manipulator consists of two linear stages (Xslide, Velmex Inc.), a push-actuator (L12-R, Actuonix Motion Devices), and a motor (Dynamixel XL430-W250-T, ROBOTIS Inc.). The push actuator is installed on the motor, and the push actuator-motor assembly is connected to the two linear stages.

The strut storage holds the struts along its perimeter. A strut holding feature is mounted on the motor (Dynamixel XL430-W250-T, ROBOTIS Inc.). Once the manipulator picks up the strut, the strut storage rotates to bring the next strut to the pick-up position. Note that the sleeve installed at the center of each strut contains a small permanent magnet. The electromagnet on the tip of the manipulator interacts with this permanent magnet to hold and release the strut as the construction proceeds. The geometry of the sleeve matches the manipulator tip, to prevent rotation of the strut during the manipulator maneuver.

Two end fixtures at the exit of the truss builder with embedded electromagnets, hold the released truss bay once it is detached from the assembly plate, providing clearance to retract the assembly plate. The truss builder prototype is manufactured based on the design described above, and presented in Fig. 10b, and c.

C. Design of magnets

The reflector assembly process involves the sequential operation of the manipulator and requires several interactions between electromagnets and permanent magnets. The following is the detailed procedure for the bay construction and release: once the truss construction is initiated, the manipulator picks up joints and places them on the mounting plate. Each joint contains a permanent magnet in its body; therefore, during the bay construction, an electromagnetic force holds the joints at the right locations. After placing the joints, the manipulator picks up the strut from the storage and places it between corresponding joints. When the bay is completed, the assembly plate slides out and the polarity of the electromagnets is reversed to detach the joints from the mounting plate. Note that in the configuration where the assembly plate is fully pushed out of the truss builder, the two joints (upper and lower) on the left side of the bay are

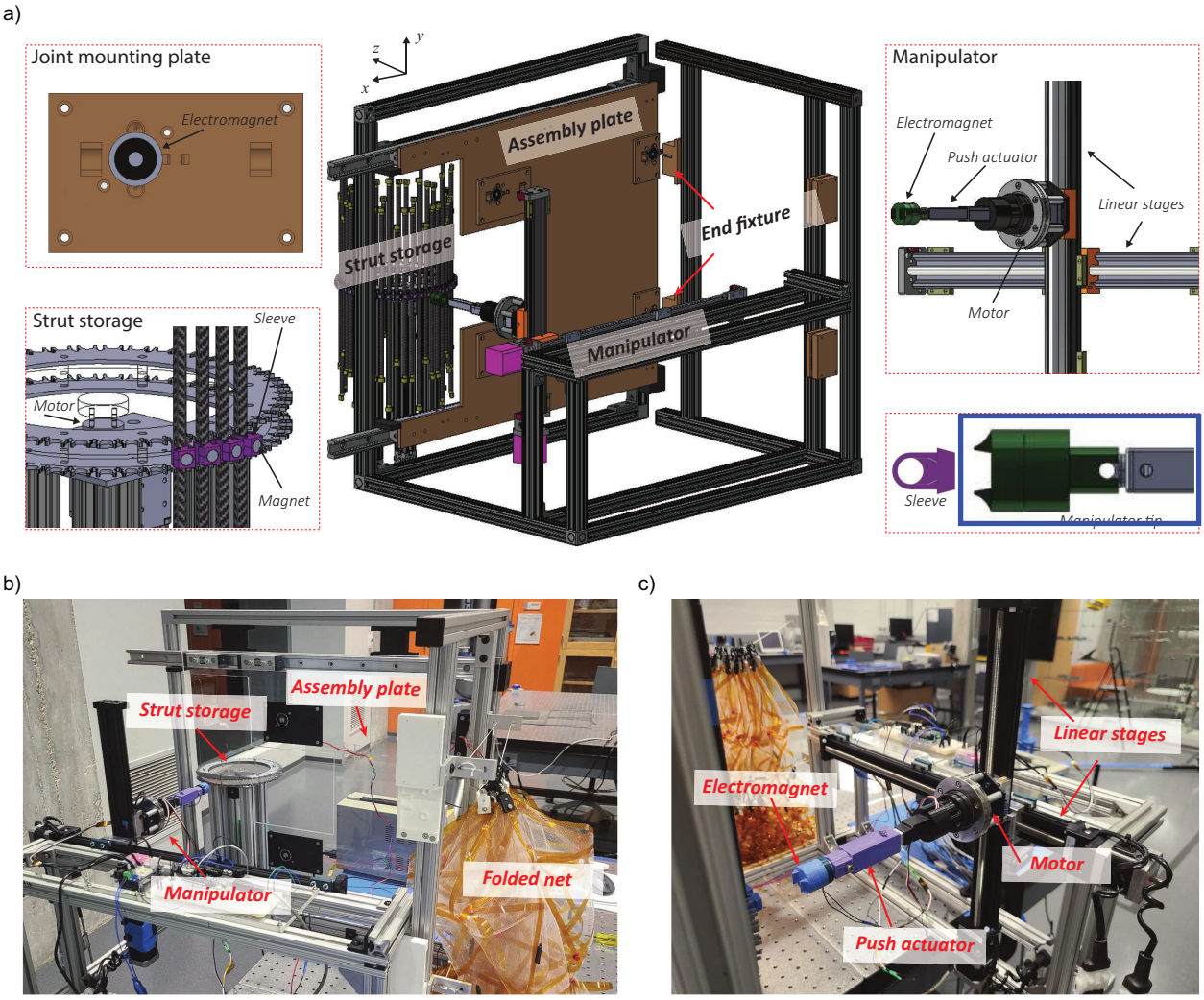

Fig. 10 Truss builder prototype: a) CAD image of truss builder and components, b) view of prototype truss builder and c) manipulator

aligned with the two end fixtures at the edge of the truss builder. Thus, when the electromagnet on the mounting plates is reversed, the joints are transferred to the end fixture where they are held by electromagnetic forces. Then, once the assembly plate has been retracted inside the truss builder, the polarity of the two electromagnets on the end fixtures is reversed, and the joints are transferred to the mounting plate.

As described in the bay construction and release process, the switching of the joint position between the mounting plate and the end fixture is required for the entire reflector assembly process. Switching the polarity of the electromagnets is the key to this process, as each electromagnet in the system attracts or repels the permanent magnets; the level of the magnetic force depends on the distance between an electromagnet and a permanent magnet. Therefore, the gap distances between the magnets are carefully designed for all of the desired operations in the assembly process to be successful. Specifically, the following conditions should be satisfied at each step of the bay construction and release process:

1) The manipulator can pick up the strut by overcoming the strut-holding force of the storage.
2) The strut should not be detached from the joint when the manipulator releases the strut.
3) Joints should not be detached from the mounting plate when the manipulator releases the strut.
4) The attraction of the end fixture should be stronger than the mounting plate when transferring the joint to the end fixture.
5) The attraction of the mounting plate should be stronger than that of the end fixture when placing back the joint on the mounting plate.

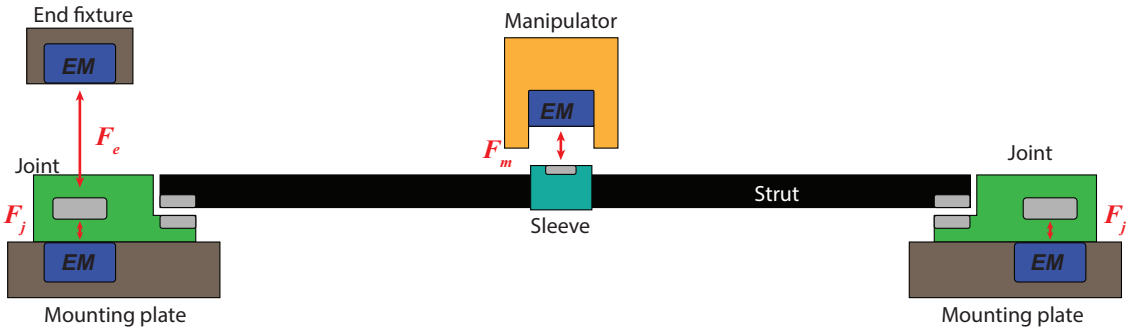

Fig. 11 Schematic drawing of the bay construction showing force interaction

Figure 11 shows a schematic drawing of the system and all the magnetic force interactions between electromagnets and the permanent magnet. In the drawing, F_m denotes the electromagnetic force between the manipulator and the magnet on the sleeve; F_e and F_j represent the electromagnetic forces of joint-end fixture, and joint-mounting plate, respectively.

Based on the conditions listed above, the following inequalities are established:

$$F_{m+} > 2.10\ N \tag{5}$$

$$F_{m-} < 5.38\ N \tag{6}$$

$$F_{m-} < Min(2F_{j+}, 2F_{j+} - 2F_{e-}) \tag{7}$$

$$F_{j-} < F_{e+} \tag{8}$$

$$F_{e-} < F_{j+} \tag{9}$$

The strut holding force from the storage and the attraction force between two permanent magnets in the strut tip and joint slot are experimentally measured as 2.10 N and 2.69 N, respectively. The electromagnetic force can be expressed as a function of the voltage (V), and the distance (d) to the subject (i.e., $F_{em} = f(d, V)$); the positive, and negative symbols in the subscript of the electromagnetic forces correspond to the maximum (+12 V applied) and minimum (-12 V applied) force generated from the electromagnet at given distance, respectively. To evaluate the stability of the system to correctly operate as described, the safety factors for each step are defined based on inequalities (Eqs. 5 - 9):

$$S.F.1 = \frac{F_{m+}}{2.1} \tag{10}$$

$$S.F.2 = \frac{5.38}{F_{m-}} \tag{11}$$

$$S.F.3 = \frac{2Min\left(F_{j+}, F_{j+} - F_{e-}\right)}{F_{m-}} \tag{12}$$

$$S.F.4 = 1 + \text{sgn}\left(F_{e+} - F_{j-}\right)\frac{\left|F_{e+} - F_{j-}\right|}{\sqrt{2}} \tag{13}$$

$$S.F.5 = 1 + \text{sgn}\left(F_{j+} - F_{e-}\right)\frac{\left|F_{j+} - F_{e-}\right|}{\sqrt{2}} \tag{14}$$

Note that a safety factor below 1 means the corresponding part of the assembly process has failed. Figure 12a presents the variation of the design parameters of the system regarding the distance between electromagnets and permanent magnets: the gap between the manipulator and the sleeve is denoted by d_m, while d_j, d_e, and d_g are the distance between the permanent magnet and mounting plate, joint top surface, and end fixture, respectively.

To analyze the effect of the design parameters on the system operation, we experimentally measured the variation of the force of the electromagnet with the distance to the permanent magnet, and established Eqs. 10 - 14. Each safety factor is analyzed by varying design parameters, starting from the reference design point (d_m = 1.2 mm, d_j = 3.5 mm, d_e = 3.5 mm, d_g = 3.5 mm) in the range -50 % to +50 %.

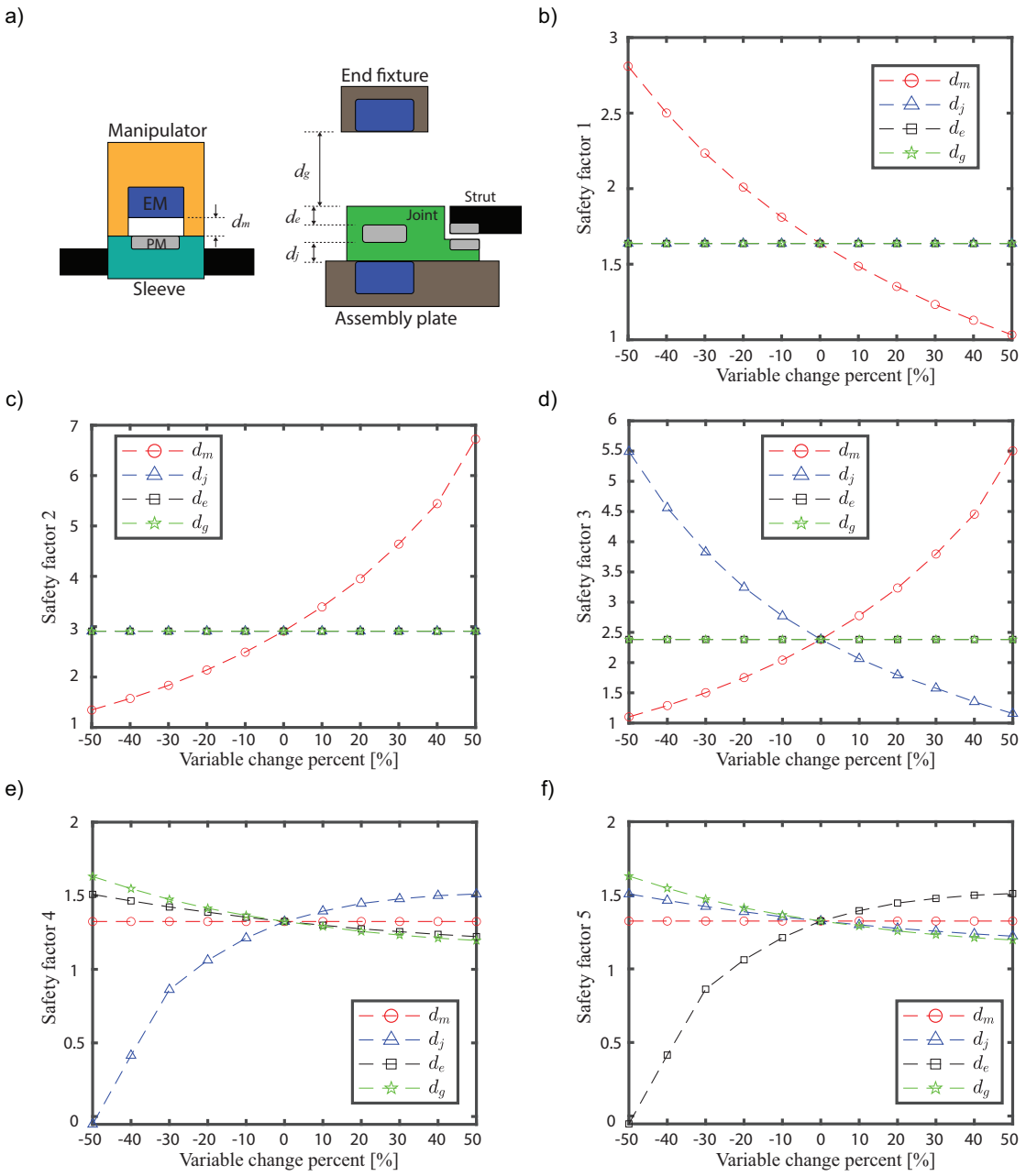

Fig. 12 Sensitivity analysis: a) design parameters, b) Safety factor 1, c) Safety factor 2, d) Safety factor 3, e) Safety factor 4, and f) Safety factor 5

Figures 12b-f show the sensitivity analysis results for each safety factor. These results clearly show the complicated inter-relations between the design parameters for each assembly process: Safety Factors 1 and 2 are affected only by d_m showing opposite tendencies for varying d_m. Safety factor 3 increases for increasing d_m and decreasing d_g. Note that Safety Factors 4 and 5 are affected by d_m and d_g in the same manner. However, d_e and d_j show opposite tendencies against the joint transferring direction, thus it is essential to find the optimal value for the design parameters completing all operations successfully.

To find the optimal design, the following objective function is defined:

$$f\left(d_m, d_j, d_e, d_g\right) = (S.F.1 - 1.5)^2 + (S.F.2 - 1.5)^2 + (S.F.3 - 1.5)^2 + 5(S.F.4 - 1.5)^2 + 5(S.F.5 - 1.5)^2 \quad (15)$$

The optimal values for each design parameter are obtained by minimizing the established objective function. The result of the optimization is $[d_m, d_j, d_e, d_g]_{opt} = [1.0, 4.1, 4.2, 4.0]$ mm, which corresponds to safety factors [1.9, 2.3, 1.4, 1.5, 1.5]. This is the design that has been implemented in the truss builder prototype.

D. Prototype reflector assembly demonstration

The assembly process has been demonstrated using the prototype reflector parts and the truss builder. Figures 13a-d show the assembled reflector at the following steps: (a) start of the operation, (b) 5 bays constructed, (c) 8 bays constructed, and (d) completed configuration. Through the assembly demonstration, it was confirmed that the reflector assembly can be completed through operations carried out inside the truss builder. By implementing the optimized design parameters for the truss builder system obtained from the design sensitivity analysis, each step in the bay construction and release was completed successfully. Note that the folded net is gradually deployed along with the perimeter truss, as the diameter of the truss grows by adding more bays to the reflector. The completed reflector is presented in Fig. 13e.

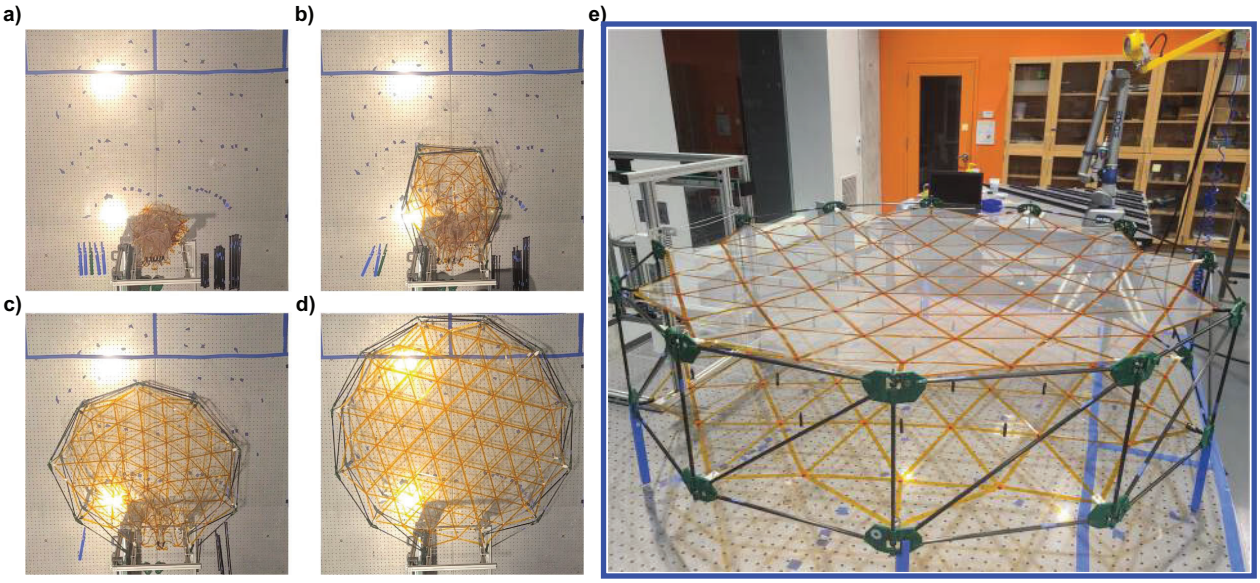

Fig. 13 Reflector assembly demonstration: a) initial state, b) 5-bay constructed, c) 8-bay constructed, d) assembly completed, and e) assembled reflector prototype

VI. Conclusion

This study has presented a scheme for robotically assembling large reflectors, based on the AstroMesh reflector architecture. The geometry and structural design have been presented, and the mass and stowed volume of the reflector have been determined for aperture diameters up to D = 200 m. This study has shown the potential advantages of in-space assembled reflectors compared to traditional deployable designs, especially the reduction of the required launch envelope.

An in-space assembly scheme has been presented for the chosen reflector architecture: the key is a truss builder facility launched into orbit with the structural components, and simple robots. The truss builder conducts the complete reflector assembly by repeating the following sequence of operations: i) construct a bay of the perimeter truss; ii) attach the outer node of the cable net to the bay; and iii) push the constructed bay out of the truss builder. The detailed procedure for bay construction and release was also established, and discussed.

A proof-of-concept demonstrator was built to verify the feasibility of the concept in all steps of operation. The structural components of the prototype reflector were designed modularly to be assembled by simple robots. A prototype

reflector with $D = 1.4$ m was manufactured mainly with additive manufacturing techniques. This prototype was used to perform the bay construction and release operation. Most of the construction steps require the interaction between electromagnets and permanent magnets. Therefore, the design parameters that affect the electromagnetic forces were identified and analyzed in a sensitivity study of the system. The optimal values for successful operation were then obtained, and implemented in the prototype truss builder design. A proof-of-concept demonstration was performed to build the prototype reflector through the truss builder manufactured in this study. An assembly demonstration has been conducted successfully, confirming the feasibility of the proposed in-space assembly scheme for large mesh reflectors.

Acknowledgments

This research was funded by the DARPA NOM4D program directed by Dr. Andrew Detor, under grant HR001122C0054.

References

[1] Puig, L., Barton, A., and Rando, N., "A review on large deployable structures for astrophysics missions," *Acta Astronautica*, Vol. 67, No. 1-2, 2010, pp. 12–26. https://doi.org/10.1016/j.actaastro.2010.02.021.

[2] Agnes, G., "Precision deployable structures technology for NASA large aperture missions," *Space 2004 Conference and Exhibit*, 2004, p. 5899. https://doi.org/10.2514/6.2004-5899.

[3] Gdoutos, E., Sommer, C. F., Truong, A., Wen, A., Pedivellano, A., Ubamanyu, K., Madonna, R. G., and Pellegrino, S., "Development of the Deployable on-Orbit ultraLight Composite Experiment (DOLCE) for the Space Solar Power Project Demonstration Mission," *AIAA SciTech 2022 Forum*, 2022, p. 1266. https://doi.org/10.2514/6.2022-1266.

[4] Hedgepeth, J. M., "Influence of fabrication tolerances on the surface accuracy of large antenna structures," *AIAA Journal*, Vol. 20, No. 5, 1982, pp. 680–686. https://doi.org/10.2514/3.7936.

[5] Thomson, M. W., "The Astromesh deployable reflector," *IEEE Antennas and Propagation Society International Symposium. 1999 Digest. Held in conjunction with: USNC/URSI National Radio Science Meeting (Cat. No. 99CH37010)*, Vol. 3, IEEE, 1999, pp. 1516–1519. https://doi.org/10.1109/APS.1999.838231.

[6] Thomson, M., "AstroMesh deployable reflectors for Ku and Ka band commercial satellites," *20th AIAA International Communication Satellite Systems Conference and Exhibit*, 2002, p. 2032. https://doi.org/10.2514/6.2002-2032.

[7] Smith, T., Lee, B., Semler, D., and Chae, D., "A large S-band antenna for a mobile satellite," *Space 2004 Conference and Exhibit*, 2004, p. 6120. https://doi.org/10.2514/6.2004-6120.

[8] Entekhabi, D., Njoku, E. G., O'neill, P. E., Kellogg, K. H., Crow, W. T., Edelstein, W. N., Entin, J. K., Goodman, S. D., Jackson, T. J., Johnson, J., et al., "The soil moisture active passive (SMAP) mission," *Proceedings of the IEEE*, Vol. 98, No. 5, 2010, pp. 704–716. https://doi.org/10.1109/JPROC.2010.2043918.

[9] Miura, K., and Pellegrino, S., *Forms and Concepts for Lightweight Structures*, Cambridge University Press, 2020. https://doi.org/10.1017/9781139048569.

[10] Zhihui, X., Jinguo, L., Chenchen, W., and Yuchuang, T., "Review of in-space assembly technologies," *Chinese Journal of Aeronautics*, Vol. 34, No. 11, 2021, pp. 21–47. https://doi.org/10.1016/j.cja.2020.09.043.

[11] Whittaker, W., Urmson, C., Staritz, P., Kennedy, B., and Ambrose, R., "Robotics for assembly, inspection, and maintenance of space macrofacilities," *AIAA Space*, Vol. 2000, Citeseer, 2000, pp. 1–6.

[12] Nishida, S.-i., and Yoshikawa, T., "A new end-effector for on-orbit assembly of a large reflector," *2006 9th International Conference on Control, Automation, Robotics and Vision*, IEEE, 2006, pp. 1–6. https://doi.org/10.1109/ICARCV.2006.345414.

[13] Lee, N. N., Burdick, J. W., Backes, P., Pellegrino, S., Hogstrom, K., Fuller, C., Kennedy, B., Kim, J., Mukherjee, R., Seubert, C., and Wu, Y.-H., "Architecture for in-space robotic assembly of a modular space telescope," *Journal of Astronomical Telescopes, Instruments, and Systems*, Vol. 2, No. 4, 2016, p. 041207. https://doi.org/10.1117/1.JATIS.2.4.041207.

[14] Miller, D. W., Mohan, S., and Budinoff, J., "Assembly of a large modular optical telescope (ALMOST)," *Space Telescopes and Instrumentation 2008: Optical, Infrared, and Millimeter*, Vol. 7010, SPIE, 2008, pp. 717–727. https://doi.org/10.1117/12.788566.

[15] Agrawal, P., Anderson, M., and Card, M., "Preliminary design of large reflectors with flat facets," *IEEE Transactions on Antennas and Propagation*, Vol. 29, No. 4, 1981, pp. 688–694. https://doi.org/10.1109/TAP.1981.1142631.

[16] Tan, L. T., and Pellegrino, S., "Thin-shell deployable reflectors with collapsible stiffeners Part 1: approach," *AIAA Journal*, Vol. 44, No. 11, 2006, pp. 2515–2523. https://doi.org/10.2514/1.16320.

[17] *M55J High modulus carbon fiber*, Toray Composite Materials America, Inc., January 2020. Rev. 2.0.

[18] *Falcon User's Guide*, SpaceX, September 2021.

[19] *Starship Users Guide*, SpaceX, March 2020.